MAUSAM, **54**, 1 (January 2003), 51- 66

551.501.776:551.501.795:551.553.21

Determination of cloud and precipitation characteristics in the monsoon region using satellite microwave and infrared observations

GUOSHENG LIU

Florida State University, Tallahassee, Florida, 32306, USA

e mail : liug@met.fsu.edu

सार – उपग्रह सूक्ष्मतरंग और अवरक्त प्रेक्षणों के आधार पर भारतीय ग्रीष्मकालीन मानसून क्षेत्र में हमने मेघ और वर्षण के लक्षणों का अध्ययन किया है। इसमें स्तरीय और संवहनीय वर्षा तथा स्थल में और महासागरों में वर्षा के मध्य भिन्नता का मुख्य रूप से अध्ययन किया गया है। जिस क्षेत्र का अध्ययन किया गया है उसमें, संवहनीय मेघों की वर्षा की औसत दर स्तरीय मेघों की तुलना में छह गुना अधिक है जबकि स्तरीय मेघों की तुलना में 4 से 5 गुना अधिक क्षेत्र में फैले होते हैं। परिणामस्वरूप, संवहनीय मेघ स्तरीय मेघों की तुलना में अधिक वर्षा करते हैं जिसका अनुपात 3:2 है। संवहनीय और स्तरीय वर्षा के मध्य भिन्नता वस्तुतः किसी भी उपग्रह से प्राप्त संकेतों – मेघशीर्ष तापमान और सूक्ष्मतरंग उत्सर्जन, प्रकीर्णन और संयुक्त संकेतों से स्पष्ट हो जाती है। स्तरीय वर्षा के संबंध में मेघशीर्ष तापमान सतही वर्षा की दरों को दर्शाने में सहायक नहीं होते हैं जबकि मेघ–शीर्ष के शीतल तापमान से संवहनीय मेघों में वर्षा की दर अधिक हो जाती है। वर्षा की दर में वृद्धि के साथ संवहनीय वर्षा की तुलना में स्तरीय वर्षा में सूक्ष्मतरंग उत्सर्जन संकेत अधिक जल्दी बहुत अधिक तक पहुँच जाता है। संवहनीय वर्षा के संबंध में, वर्षा दर प्रकीर्णन संकेत संबंध से स्थल और महासागर में होने वाली वर्षा में विशेष भिन्नता का पता चलता है। समान वर्षा दर के अनुरूप, महासागर की तुलना में स्थल में प्रकीर्णन संकेत लगभग दोगुना अधिक होते हैं। औसत उर्ध्वाधर वर्षण प्रोफाइलों से पता चला कि हिमांक तल से स्तरीय वर्षा की दर समान रही और उससे ऊपर तीव्र ड्राप ऑफ रहा चाहे स्थल में हो या महासागर में। दूसरी ओर, संवहनीय वर्षा प्रोफाइल के हिमांक तल से नीचे प्रायः वर्षा की दर अधिकतम रही जो संलयन जैसे उष्ण सूक्ष्मभौतिकीय प्रक्रियाओं द्वारा वर्षा में महत्वपूर्ण वृद्धि दर्शाते हैं। यह भी देखा गया है कि समान सतही वर्षा दर के होते हुए संवहनीय वर्षा के संबंध में, हिमांक तल से ऊपर हिमकणों की मात्रा महासागर की तुलना में स्थल में पर्याप्त मात्रा से अधिक होती है जिससे दो भिन्न प्रकार की सतहों में होने वाली वर्षा के मध्य प्रकीर्णन संकेतों में भिन्नता का पता चलता है। इसमें यह भी बताया गया है कि समतल – समानान्तर निदर्श अनुकारों और वास्तविक उपग्रह से लिए गए प्रेक्षणों के बीच मेल न होना ही वर्षा की उप–पिक्सेल परिवर्तिता के लिए उत्तरदायी है।

ABSTRACT. We have studied the cloud and precipitation features in the Indian summer monsoon region based on satellite microwave and infrared observations. Emphases are particularly given to the differences between stratiform and convective rains and between rains over land and over ocean. In the studied region, average rainfall rate of convective clouds is about 6 times higher than for stratiform clouds while the latter covers 4 to 5 times more area than the former. As a result, convective rains produce higher rain total than stratiform rains with a ratio of about 3 : 2. The difference between convective and stratiform rains is evident virtually by any satellite signatures – cloud top temperature, and microwave emission, scattering and combined signatures. Cloud top temperature appears no skill to reflect surface rainfall rates for stratiform rains while colder cloud top temperatures correspond to higher rainfall rates for convective clouds. As rainfall rate increases, microwave emission signature reaches saturation much quicker for stratiform rains than for convective rains. For convective rains, the rainfall rate – scattering signature relation shows a distinct difference between rains over land and over ocean. Corresponding to the same rainfall rate, the scattering signature over land is about twice as high as that over ocean. The mean vertical precipitation profiles showed that stratiform rains have a constant rainfall rate below freezing level and a sharp drop-off above, regardless over land or ocean. Convective rain profiles, on the other hand, often have the maximum rainfall rate below the freezing level, implying a significant growth of raindrops by warm microphysical processes, such as coalescence. It is also found that given the same surface rainfall rate, the amount of ice particles above freezing level is substantially greater for convective rains over land than over ocean, which explains the difference of scattering signatures between rains over the two different surface types. It is also demonstrated that the sub-pixel variability of rains is largely responsible for the mismatch between plane-parallel model simulations and actual satellite observations.

Key words – Precipitation, Radiometer, Precipitation radar, Brightness temperature, Microwave emission signature, Microwave Scattering signature, Radiative transfer model, Plane-parallel assumption, Precipitation profile, Sub-pixel inhomogeneity, Remote sensing.

1. Introduction

Satellite remote sensing of cloud and precipitation has been playing an increasing role in weather forecasting and climate diagnostic studies (Krishnamurti *et al*., 2001; Rossow and Schiffer, 1991; Ramanathan and Collins, 1991). One of the most important applications of satellite remote sensing is to determine rainfall at ground and the vertical distributions of precipitation-size particles (Wilheit *et al.*, 1994; Kummerow *et al*., 2000; Liu and Fu, 2001). The need to improve satellite retrieval of rainfall rate/amount has motivated the Tropical Rainfall Measuring Mission (TRMM, Simpson *et al*., 1988) and the Global Precipitation Climatology Project (GPCP, Arkin and Xie, 1994). Although many studies were conducted on a broad global scale, there have been very few studies on satellite cloud and rainfall retrievals with a special focus on the Indian summer monsoon region. In this study, we attempt to comprehend the cloud and precipitation characteristics in this region through interpreting satellite received microwave and infrared radiances.

Satellite remote sensing of cloud and precipitation is based on the radiative intensities emitted or reflected by cloud and precipitating hydrometeors (Liu, 2002). For active sensing by spaceborne microwave radars, the intensity of radar returns is expressed by radar reflectivity, which measures the volume backscattering by precipitation-size hydrometeors. Radar reflectivity is approximately proportional to the sixth power of mean particle size and closely related to precipitation rate. For passive sensing in the infrared and microwave wavelengths, the radiative intensity is often expressed in terms of brightness temperature, defined by the temperature that is required to match the measured intensity to the Planck blackbody function. Brightness temperature in the infrared often represents the physical temperature of the cloud top because most clouds are optically thick for infrared radiation. Microwave radiation, on the other hand, can penetrate through cloud and rain layers, and its intensity reflects the integrated contribution by all water drops and ice particles in the atmospheric column. In the visible spectrum, the measured radiative intensity is due to the reflection of sunlight by clouds and surface features. Although visible radiation has a deeper penetration than infrared radiation, visible reflectivity still represents only the top portion of clouds.

The current TRMM satellite receives all the radiative intensities mentioned above, which makes the TRMM observations extremely useful for viewing the same phenomenon with different "eyes". In this study, we examine the clouds and precipitation in the Indian summer monsoon region with the multiple spectra data using a methodology that blends observational data analyses with radiative transfer model simulation. It is attempted to understand the observed signatures by comparing them with model results. Emphases are particularly given to the differences in radiative properties between stratiform and convective rains and between rains over land and over ocean. Although no attempt is made to formulate algorithms for retrieving cloud water and precipitation, the results from this study will be very helpful to guide future algorithm development. For a comprehensive review of satellite precipitation algorithms, the readers are referred to Smith *et al*. (1998) and Adler *et al*. (2001).

The rest of the paper is arranged as follows. Section 2 describes TRMM satellite data used in this study and the rain statistics derived using TRMM radar observations for the region and time period of study. Section 3 discusses the microwave signatures of precipitation. The observed and simulated relations between rainfall and satellite signatures are presented in section 4. The vertical and horizontal structures of precipitation are presented in section 5. Lastly, the conclusions are summarized in section 6.

2. Satellite data and rain statistics

2.1. *Satellite data*

The data used for this study are from observations of the TRMM satellite, including data from the precipitation radar (PR), the TRMM microwave imager (TMI) and the visible/infrared imager (VIRS). The TRMM PR is an electronically scanning radar operating at 13.8 GHz. It scans ±17° from nadir with 49 positions, resulting in a 220-km swath width and a horizontal resolution of 4.3 km at nadir. The vertical resolution of the PR data is 250 m. The sensitivity of the radar is such that the minimum detectable signal is about 20 dBZ, which corresponds to about 0.7 mm h^{-1} in rainfall rate. The TRMM standard 2A25 product of attenuation-corrected precipitation profiles is used for this study. The vertical profiles of rainfall rate R are calculated from the radar reflectivity Z profiles by using a Z-R relationship based on a hybrid of the Hitschfeld-Bordan method and the surface reference method (Iguchi and Meneghini, 1994). Rainfalls are classified into three types based on the vertical pattern of the profiles. A precipitation profile is classified as stratiform if the PR detects a bright band near the freezing level. If no bright band exists and any value of the attenuation-corrected radar reflectivity in the beam exceeds a predetermined value of ~39 dBZ, the profile is classified as convective. Profiles are labeled "others" when they do not meet the definitions of either stratiform or convective rain (Awaka *et al*., 1998). We found that

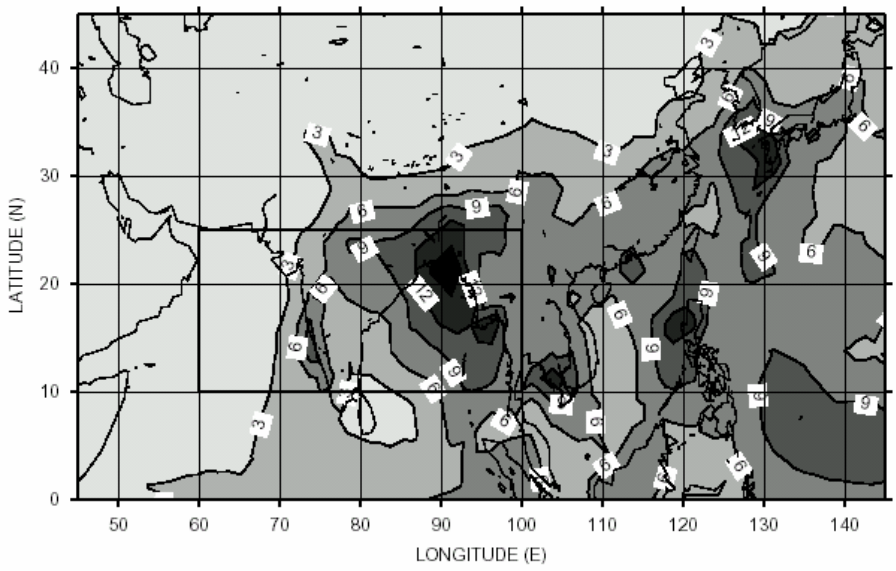

Fig. 1. Mean rainfall rate (mm day^{-1}) during 1 June to 30 September 1999 produced using GPCP data. The region focused by this study is indicated by the box

only ~0.2% of the profiles belongs to "others" in the region and time period we analyzed. Therefore, we'll ignore this type in this study. Due to surface reflection, radar reflectivities at the levels near the surface are contaminated, particularly for land areas (Note: the altitude used in the profiles is height above sea level). For this reason, we will use rainfall rates at 2-km altitude above sea level as "surface rainfall rate".

The TMI is a conically scanning microwave radiometer that measures brightness temperatures at the following five frequencies: 10.7, 19.4, 21.3, 37.0 and 85.5 GHz. Dual polarizations are measured at all frequencies except for 21.3 GHz, at which only vertical polarization is observed. The TMI sampling swath width is 720 km across the earth's surface, with individual pixel spatial resolution ranging from 39 km at 10.7 GHz to 4.4 km at 85.5 GHz. The TRMM standard product 1B11 used in this study contains the calibrated and navigated brightness temperatures. The VIRS instrument is a cross-scanning radiometer receiving radiances at the following five wavelengths: 0.63, 1.61, 3.75, 10.8, and 12.0 μm. Brightness temperatures from 10.8 μm channel of VIRS 1B01 data are used in this study to infer cloud top temperature. The VIRS scans ± 45° from nadir resulting in a swath width of 720 km. Its spatial resolution is ~ 2 km at nadir.

To determine the relationships of rainfall rate *versus* satellite infrared and microwave radiation signatures, we generated a spatially and temporally collocated TMI and PR dataset with the resolution of TMI 19.4 GHz data (~25 km), and a collocated PR and VIRS dataset with the resolution of PR data (~5 km). To reduce spatial mismatch of these sensors caused by different viewing geometries, the collocation was conducted only for nadir pixels. The collocation between TMI and PR is described as follows, and the collocation between PR and VIRS data is conducted in a similar fashion. For a given TMI pixel, we first select the PR pixels that have a distance between their center and the center of the TMI pixel shorter than 0.125° (latitude/longitude), which is about one-half of the footprint size of the 19.4 GHz channel. The mean rainfall rate over the TMI pixel is derived by a weighted average of observations at these selected PR pixels. The weight assigned to a selected PR pixel decreases with the distance of its center to the center of the TMI pixel following the function $\exp(-x/2\sigma^2)$, where x is the distance and σ is a constant that can be determined by letting the weight reduce to one-half when x increases from 0 to 0.125°. The weights are then normalized so that the sum of the weights of all selected PR pixels is equal to unity. This collocation procedure is effectively a resampling of the PR rainfall rate at the location and resolution of the TMI 19.4 GHz pixel by using rainfall rates of the surrounding PR pixels and by assuming that the radar has a Gaussian antenna pattern. Similarly, infrared brightness temperatures from VIRS are resampled at the location and spatial resolution of PR pixel to generate a collocated PR-VIRS dataset.

2.2. *Rain statistics in the region and time period of study*

Our interests of study are for the Indian monsoon region during summer monsoon months. The rainfall

TABLE 1

Statistics of precipitation in the monsoon region

	Ocean		Land	
	Convective	Stratiform	Convective	Stratiform
Area fraction	1.2%	5.0%	1.5%	7.6%
Rain fraction	59%	41%	54%	46%
Mean rainrate	9.5 mm h^{-1}	1.6 mm h^{-1}	9.5 mm h^{-1}	1.6 mm h^{-1}

TABLE 2

Simplified form of the right-hand side of Eqn. (1)

	Over Land (ε_s~1)	Over Ocean
Low frequency	T_s	$T_s[1-e^{-2\tau_w}(1-\varepsilon_s)]$
High frequency	$T_s e^{-\tau_i}$	$T_s e^{-\tau_i}$

distribution for the period of 1 June through 30 September 1999 is shown in Fig. 1 for the region of 0° - 45° N, 45° - 145° E. The diagram is generated using monthly precipitation data from the GPCP archived by NASA (Huffman *et al*., 1995), which are merged product of raingauge measurements, satellite retrievals and numerical model outputs. It is seen that the Indian summer monsoon has a strong signature in the rainfall field, with the rainfall rate maximum observed near the coastal region of the Bay of Bengal. Our analyses in this study will focus on this rainy region as indicated by solid line box in Fig. 1, which covers 10° N to 25° N and 60° E to 100° E. We will refer this region as "monsoon region" hereafter.

The precipitation statistics derived from TRMM PR rainfall data during 1 June to 30 September 1999 for the monsoon region are given in Table 1. The classification of stratiform and convective rain types has been done by Awaka *et al.* (1998) as described in section 2.1. The rain type information is included in the PR 2A25 products. The area fraction is the number ratio of pixels of a specific rain type (stratiform or convective) to all pixels including raining and non-raining pixels. Similarly, the rain fraction is the ratio of rain amount generated by a specific rain type to total rain amount. On average, rains cover about 6 to 9% of the entire area with slightly larger area fraction over land than over ocean. Stratiform rain area is about 4~5 times larger than the convective rain area. However, because of the higher rainfall rate, convective clouds generate more rain amount than stratiform clouds regardless over ocean or over land. The ratio is about 3:2. The averaged rainfall rate for convections is ~9.5 mm h^{-1} while it is only ~1.6 mm h^{-1} for stratiform rains. Keeping these statistics in mind, we next present the microwave and infrared signatures of these rain clouds and their structures.

3. Microwave emission and scattering signatures

Microwave signals measured from a satellite-borne radiometer can be generally classified into two categories based on how the microwave field interacts with the atmospheric hydrometeors : emission and scattering. To understand the microwave emission and scattering signatures, let us consider an idealized rain cloud that contains raindrops below freezing level and ice particles above. Although accurate estimation of satellite-received radiances requires solving a radiative transfer model with the consideration of absorption and multiple scattering (Liu, 1998), the primary radiative signature may be understood by examining the following crude approximation (Liu, 2002) :

$$T_B = T_s[1-e^{-2\tau_w}(1-\varepsilon_s)]e^{-\tau_i}, \qquad (1)$$

where T_B is the brightness temperature received by a radiometer on the satellite, T_s and ε_s are, respectively, the surface temperature in Kelvin and the surface emissivity, τ_w and τ_i are, respectively, the optical depth for the raindrops and ice particles. For simplicity, emission from atmospheric gases is ignored in Eqn. (1) because our primary concern here is the signature from clouds and precipitation. However, the atmospheric gases' emission is an important contribution to the microwave radiation, especially near water vapor and oxygen absorbing frequencies.

Depending on the frequency of the radiation received and whether the surface is land or ocean, we may further simplify Eqn. (1) as shown in Table 2, in which the following assumptions are used :

(*i*) Over land, surface emissivity is close to unity, *i.e.*, $\varepsilon_s \sim 1$.

(*ii*) For low frequency microwaves, ice clouds are transparent, *i.e.*, $\tau_i \sim 0$.

(*iii*) For high frequency microwaves, rain layers are opaque, *i.e.*, $\tau_w \to \infty$.

These assumptions are generally valid for low and middle latitude conditions. At high latitudes, particularly during winter, the rain layer becomes very shallow, or even no rain layer at all (*i.e.*, snowfall); the last assumption then becomes invalid.

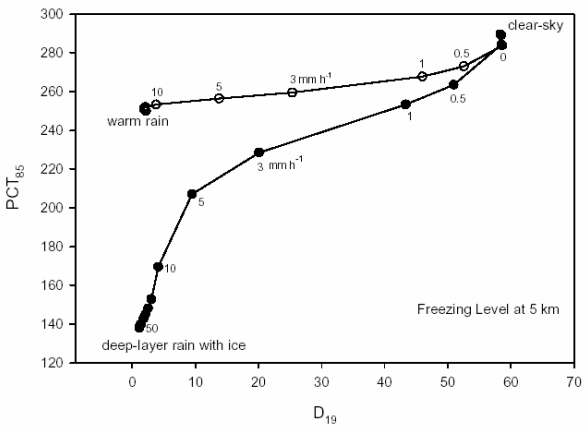

Fig. 2. Relation between microwave emission (D_{19}) and scattering signatures (PCT_{85}) as simulated by a radiative transfer model. A warm rain case (open circles) and a deep-layer rain case (solid circles) are presented. The corresponding surface rainfall rates are indicated by numbers aside the points

From Table 2, it becomes immediately obvious that no atmospheric information can be detected at low frequency microwaves over land. Over ocean at low frequency microwaves, the brightness temperature varies with τ_w, the optical depth resulted from raindrops. The more the raindrops exist in the atmosphere, the larger the optical depth is, and in turn, the higher the brightness temperature will be. The signature reflects the intensity of the microwave emission from liquid water drops; therefore, is called emission signature. At high frequency, on the other hand, the brightness temperature varies with τ_i, the optical depth resulted from ice particles. A higher concentration of ice particles leads to a greater optical depth and a lower brightness temperature. Since the decrease in satellite received radiation is caused by the scattering of ice particles, this signature at high frequency microwaves is called scattering signature.

Although brightness temperatures at low and high frequencies can be used to represent emission and scattering signatures, respectively, the relation between brightness temperature and rainfall rate or column water path often show heavily bended curves (Wilheit *et al*., 1977 ; Spencer *et al*., 1989; Liu and Curry, 1993); so given a value of rainfall rate or water path brightness temperature could have two corresponding values. To avoid this problem, parameters that use a function of brightness temperatures from multiple channels are defined to represent the emission and scattering signatures (Spencer *et al*., 1989; Petty, 1994; Liu and Curry, 1998). Here, we use the definitions of Liu and Curry (1998). The emission signature is defined by the polarization difference of brightness temperatures at a low frequency (19.4 GHz), *i.e*., $D = T_{BV}–T_{BH}$, where the subscripts *V* and *H* denote vertical and horizontal polarizations, respectively. From Table 2, we found that $D = \Delta\varepsilon_s T_s e^{-2\tau_w}$ over ocean, where $\Delta\varepsilon_s$ is the surface emissivity difference between vertical and horizontal polarizations. For clear-sky (τ_w=0), *D* is at its maximum. It then decreases as τ_w increases because the emission of water drops reduces the difference between vertical and horizontal brightness temperatures.

To represent the scattering signature we used the polarization corrected temperature (PCT) at a high frequency (85.5 GHz) as defined by Spencer *et al*. (1989), which is expressed by $PCT = (1+\alpha)T_{BV}-\alpha T_{BH}$, where α is coefficient designed to keep values of PCT almost constant for non precipitating conditions. Spencer *et al*. (1989) used a value of 0.818, but we will use $\alpha = 0.5$ for the summer monsoon region based on our earlier study (Liu and Curry, 1998). It is noted that PCT approaches to brightness temperature itself, as clouds become opaque to high frequency microwaves, so that $T_{BV} = T_{BH}$.

Fig. 2 shows the relationships between D_{19} and PCT_{85} simulated by a radiative transfer model, where the subscripts 19 and 85 in *D* and PCT denote frequencies in GHz. The radiative transfer model used for the calculations has been described by Liu (1998). In these calculations, we assumed a tropical standard atmosphere with the freezing level height at 5 km and an ocean surface with temperature of 300 K. Two types of rain clouds were considered: a shallow warm rain with only raindrops below freezing level and a deep-layer rain with raindrops below and ice particles above freezing level. As rainfall rate increases, D_{19} decreases; but substantial decrease in PCT_{85} only occurs for the deep-layer rain case since it contains ice particles. Therefore, the curvature in the D_{19} – PCT_{85} relation is an indication of the relative abundance of liquid versus ice in the compositions of the rain clouds. That is, the D_{19} – PCT_{85} plot for rain clouds with substantial amount of ice particles has a large curvature while the plot for rain clouds containing few ice particles is almost flat. Bearing this in mind, let's examine the D_{19} – PCT_{85} relation observed by TRMM TMI instrument as shown in Fig. 3, which are the averages of all observations during the four months from 1 June to 30 September 1999 in the monsoon region. The solid dots show the averages and the error bars show the range of $\pm\sigma$ (standard deviation).

Compared to the curves simulated by the radiative transfer model shown in Fig. 2, the observed decrease of PCT_{85} as D_{19} decreases (Fig. 3) is much more gradual than the deep-layer rain curve but steeper than the warm rain curve. For D_{19}>60 K, there is unlikely a rain event, so the small variation of D_{19} is largely caused by the variation of water vapor in the atmosphere. Significant decrease of

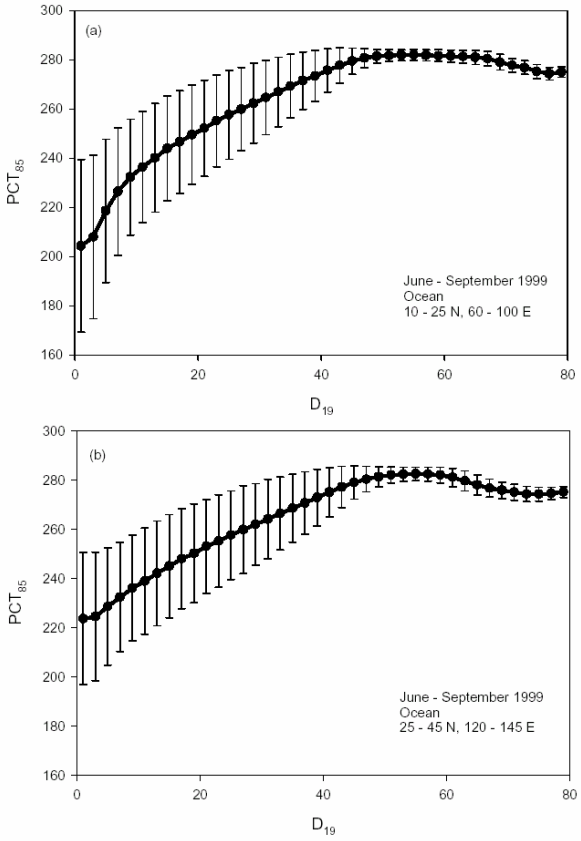

Figs. 3(a&b). Averaged relation between microwave emission (D_{19}) and scattering signatures (PCT_{85}) as observed by TMI for (a) the Indian summer monsoon region and (b) the Japan frontal region during the period of 1 June through 30 September 1999. The error bars indicate plus or minus one standard deviation

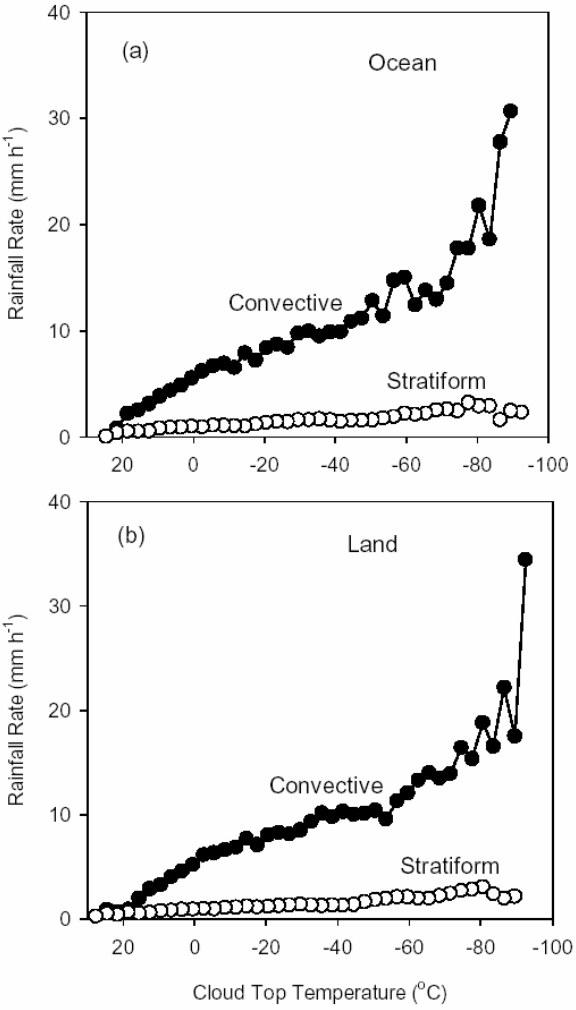

Figs. 4(a&b). VIRS cloud top temperature *versus* TRMM PR near-surface (2-km altitude) rainfall rate for rains over (a) ocean and (b) land areas averaged in the Indian summer monsoon area during 1 June through 30 September 1999. Note that the relations are very different between convective and stratiform rains

PCT_{85} occurs when D_{19} is smaller than 45 K, which corresponds to ~1 mm h^{-1} of rain according to our model simulation (Fig. 2). Two factors may have contributed to the departure of the observed from the simulated D_{19} – PCT_{85} relations. First, because of its large footprint (~25 km for 19.4 GHz), a satellite pixel contains a mixture of precipitation cells at various developing stages as well as rain-free areas. The effective radiation from this mixture is different from that simulated by a plane-parallel radiative transfer model. This effect will be further explained in section 5. Second, there may be substantial liquid water drops above freezing level in the observed clouds, which has a masking effect to the ice scattering signature, and leads to the decrease of PCT_{85} in a lesser degree. For comparison purpose, we also plotted a similar diagram in Fig.3b for a region near Japan where frontal weather systems dominate. Comparing Fig. 3(a) with Fig. 3(b), it is noticed that the PCT_{85} in southern monsoon region (10 - 25° N, 60 - 100° E) is about 20 K less than the PCT_{85} in the northern frontal region (25-45° N, 120 - 145° E) when D_{19} approaches 0, implying a stronger ice scattering by the monsoonal convective clouds than the frontal clouds. This stronger scattering could be a result of a greater number concentration, or a greater density of ice particles, or both.

An interesting finding from the diagrams is that the emission signature, D_{19}, and the scattering signature, PCT_{85}, are significantly correlated; the linear correlation coefficients for pixels with D_{19}<40 K is 0.61 for the southern monsoonal region and 0.58 for the northern frontal region. This correlation suggests that at the scale of satellite pixel a vertical column containing more raindrops is also likely to contain more ice particles aloft. While this

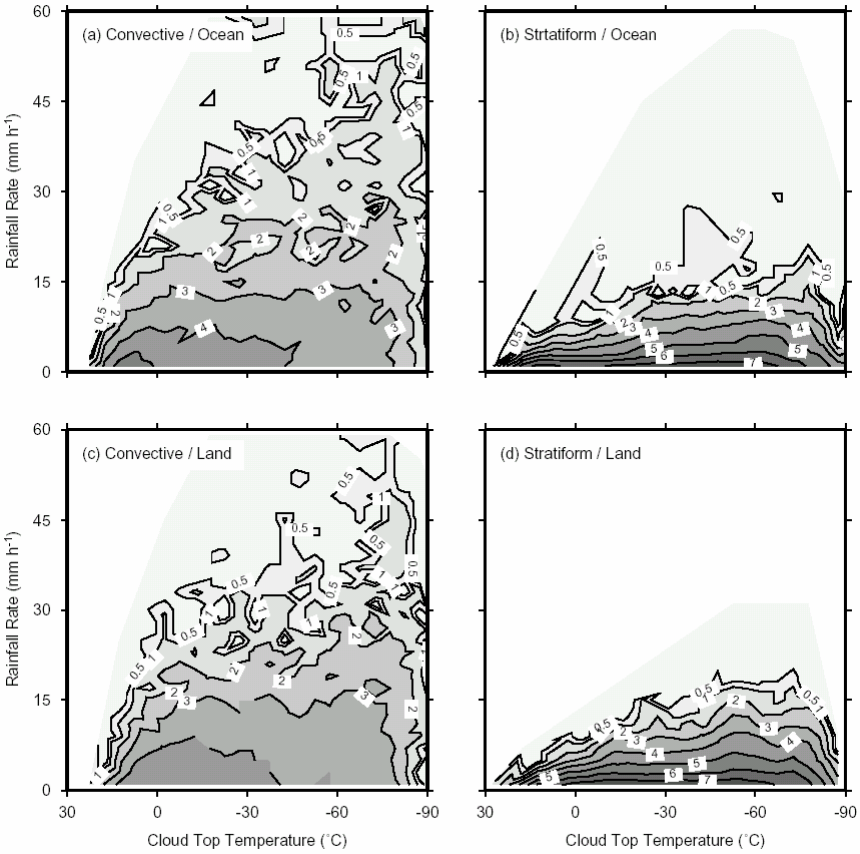

Figs. 5 (a-d). Probability distribution of raining pixels in cloud top temperature and rainfall rate space for (a) convective rain over ocean, (b) stratiform rain over ocean, (c) convective rain over land and (d) stratiform rain over land

cloud property is interesting in its own right, it is exactly this coupled nature between liquid and ice that makes it possible to estimate rainfall from microwave observations over land, where only ice scattering signatures are detectable.

4. Relations between surface rainfall and satellite observations

One of the great challenges in satellite remote sensing is how to relate the satellite observed radiances to surface rainfall rates. We investigate this relation using TRMM data. Again, the data used are from 1 June to 30 September 1999 in the region of 10° to 25° N and 60 to 100° E. We examine these relations by distinguishing whether the rain events are convective or stratiform, and whether they are over ocean or land.

4.1. *Infrared signature*

The brightness temperature from satellite infrared observations is a close proxy of cloud top temperature except for those very thin cirrus clouds that are optically too thin to be a blackbody in the infrared. For simplicity, in the following discussions we simply call the thermal infrared brightness temperature "cloud top temperature". Satellite infrared data have so far been used by many investigators for determining surface rainfall rate (Arkin and Meisner, 1987; Adler and Negri, 1988).

The relation between the infrared cloud top temperature and surface rainfall rate was derived using the collocated PR and VIRS data. Fig. 4 shows the mean relation that is derived by averaging PR surface rainfall rates at each 3-K VIRS cloud top temperature bin. The number of pixels used in producing these figures are 8230, 34604, 8108 and 41152 for convective rain over ocean, stratiform rain over ocean, convective rain over land and stratiform rain over land, respectively. For both convective and stratiform rains, cloud top temperature may reach to about -90°C (or, ~18 km in altitude). However, the corresponding mean rainfall rates for clouds with similar top height are distinctly different for convective and stratiform rains. At the coldest cloud top, the mean rainfall rate for convective rains is ~30 mm h^{-1}

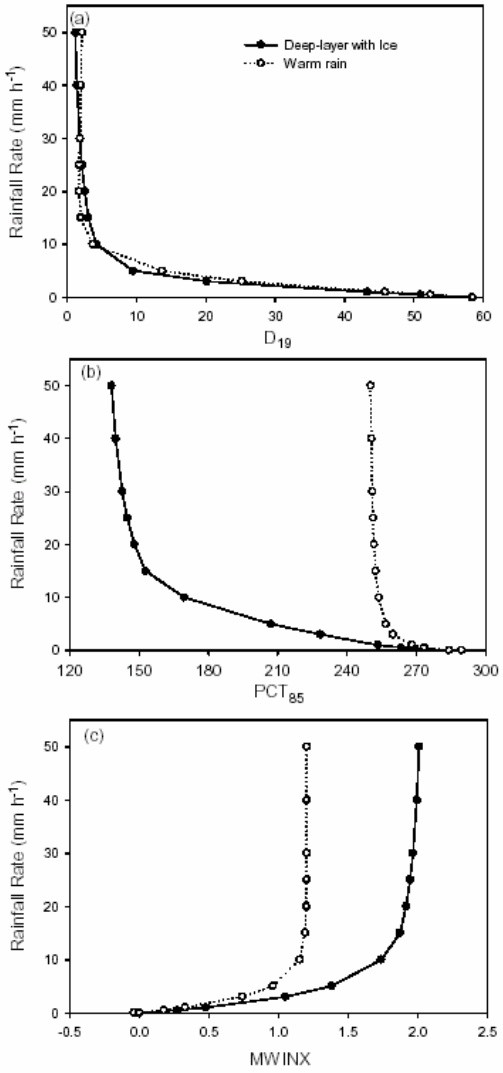

Figs. 6(a-c). Radiative transfer model simulations of rainfall rate versus (a) microwave emission (D_{19}), (b) microwave scattering (PCT_{85}) and (c) combined emission and scattering (MWINX) signatures. Dotted and solid lines respectively present the warm and the deep-layer rain cases

while it is only ~2 mm h^{-1} for stratiform rains. In fact, the plot of cloud top temperature *versus* rainfall rate for stratiform rains is so flat that it is hardly to see any correlation between the two. Also, there is no noticeable difference in these averaged relations between clouds over ocean and over land.

Although, on average, rainfall rate increases as cloud top temperature decreases as shown in Fig. 4, there is a significant variability in rainfall rates given the same cloud top temperature as demonstrated in Fig. 5, which shows the two-dimensional probability distribution of pixel occurrence. The values in the figure for drawing contours are the natural logarithm of the pixel number in a two-dimensional bin with 5-K cloud top temperature and 2 mm h^{-1} rainfall rate. For stratiform rains, most of the pixels have rainfall rate under 15 mm h^{-1}, and the high probability area spreads widely in the cloud top temperature space. For convective rains, the highest probability appears at the corner of low rainfall rate and high cloud top temperature. As cloud top temperature decreases, high probability area moves toward higher rainfall rates, resulting in a general trend of increasing rainfall rate with decreasing cloud top temperature. Again, there is no noticeable difference in these distributions between rains over ocean and over land.

4.2. *Microwave signatures*

At the microwave frequencies, the radiances received by a satellite-borne radiometer come from the entire atmospheric column of the sensor's field-of-view. Therefore, the relation between the microwave signature and surface rainfall rate depends on the three-dimensional structure of the rain field. In this section, we discuss how the microwave emission and scattering signatures as defined earlier are related to surface rainfall by both radiative transfer model simulations and satellite observations.

Fig. 6 shows the relations between microwave signatures and surface rainfall rate based on the radiative transfer simulations described in section 3. In addition to D_{19} and PCT_{85} to represent the emission and scattering signatures, we define a "microwave index" (MWINX) to represent the combined emission and scattering signature (Liu *et al*., 1995) :

$$\mathrm{MWINX} = \left(1 - D_{19} / D_{19}^{0}\right) + 2 \times \left(1 - PCT_{85} / PCT_{85}^{0}\right) \quad (2)$$

where the superscript "0" denotes D_{19} or PCT_{85} at the threshold of rain onset. As discussed in Liu *et al*. (1995), this parameter combines both emission and scattering signatures. For emission signature [(Fig.6(a)], there is little difference between deep-layer and warm rain cases in the $D_{19} - \mathrm{R}$ relation; the emission signature reaches saturation (D_{19} no longer decreases with increasing R) at ~10 mm h^{-1} of rainfall rate. The scattering signature shown in Fig. 6(b) indicates a strong response to heavier precipitations associated with deep-layer rains, while the response of PCT_{85} to warm rains is weak. The combined signature, MWINX, responds to both warm and deep-layer rains, although its sensitivity to rainfall decreases as rains become heavier.

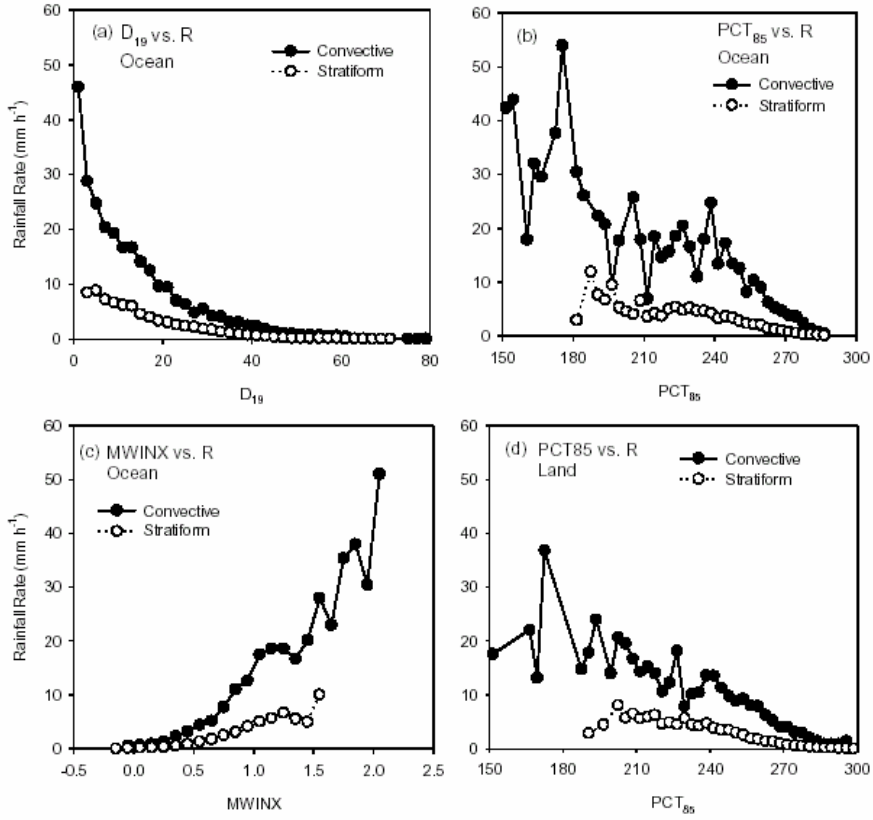

Figs. 7(a-d). Observed relations of rainfall rate *versus* (a) microwave emission (D_{19}) over ocean, (b) microwave scattering (PCT_{85}) over ocean, (c) combined emission and scattering (MWINX) over ocean and (d) microwave scattering (PCT_{85}) over land. Data are for the Indian summer monsoon region during 1 June through 30 September 1999. Note that the relations are very different between stratiform and convective rains, and between convective rains over land and over ocean

Fig. 7 shows the mean relations derived from the collocated TMI and PR data for the monsoon region during the period from 1 June to 30 September 1999. Again, we differentiated between stratiform and convective and between over ocean and over land rains. For one collocated TMI-PR pixel (~25 km resolution), we averaged several original PR pixels (~4.3 km resolution), and the rain type for these original PR pixels are often different. If more than half of the original PR pixels are convective, we will call the new collocated pixel "convective", otherwise call it "stratiform". The mean relations shown in Fig. 7 are derived by averaging those rainfall rates at 3-K D_{19}, or 5-K PCT_{85}, or 0.1 MWINX bins. The pattern of the curves in the figure is similar to those predicted by the radiative transfer model as shown in Fig. 6, but there are significant differences in the details, particularly for the PCT_{85} – R relation. The change of PCT_{85} with rainfall rate derived from the observation data over ocean [(Fig.7b) is close to, but more gradual (closer to linear) than the model simulated one for deep-layer rain case (Fig.6(b)]. For convective rains, there is a noticeable difference in the PCT_{85} – R relation between over ocean and over land. For example, at PCT_{85}~150 K, the mean rainfall rate for over ocean clouds is ~40 mm h^{-1} while it is only about 20 mm h^{-1} for over land clouds. This may be explained by the difference in precipitation profiles between oceanic and land clouds as will be shown in section 5.

There are also significant differences between convective and stratiform rains regardless surface type. Given any microwave signature, *i.e.*, D_{19}, PCT_{85}, or MWINX, mean rainfall rate for convective rains is always larger than for stratiform rains. In other words, for the same surface rainfall rate, microwave signatures for stratiform rains are stronger (smaller D_{19}, smaller PCT_{85} and bigger MWINX) than those for convective rains, although stratiform rainfall rates are generally low.

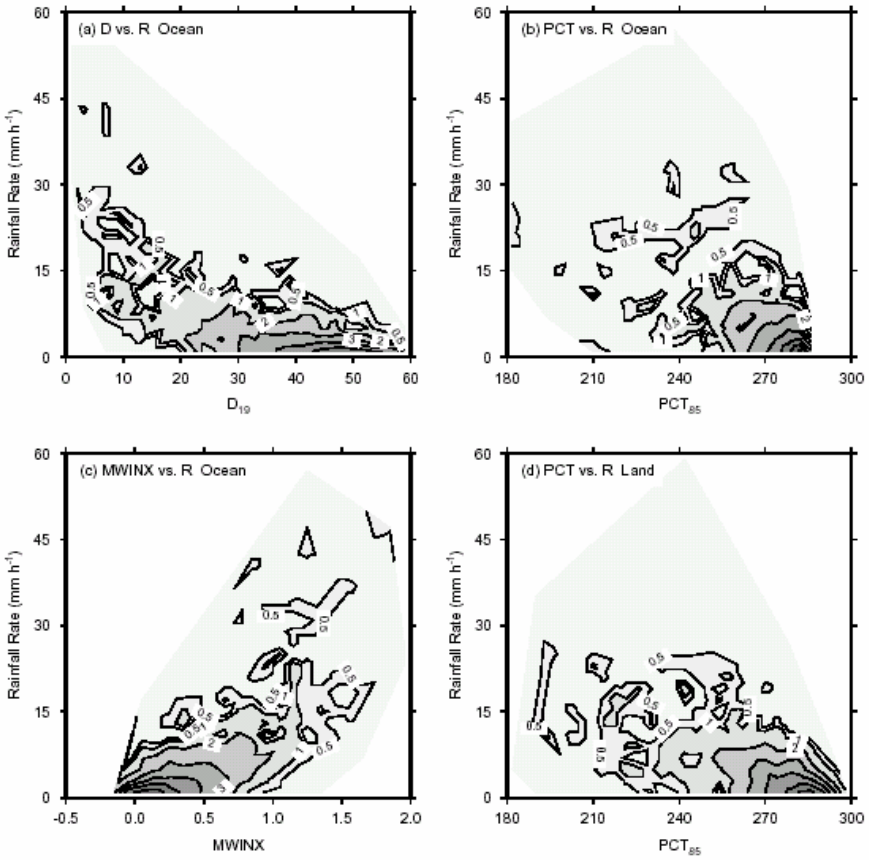

Figs. 8(a-d). Probability distribution of convective rain pixels in the space of (a) D_{19} and rainfall rate over ocean, (b) PCT_{85} and rainfall rate over ocean, (c) MWINX and rainfall rate over ocean, and (d) PCT_{85} and rainfall rate over land

What are shown in Fig. 7 are the mean relations between rainfall rate and microwave signatures. To illustrate the variability of these relations among individual pixels, the 2-dimensional probability distributions of pixel occurrence are shown in Fig. 8 for convective and in Fig. 9 for stratiform rains. The values for drawing the contours are the natural logarithm of pixel number in each 2-dimensional bin, which is 3-K by 2 mm h^{-1} for D_{19} – R plot, 5-K by 2 mm h^{-1} for PCT_{85} – R plot, and 0.1 by 2 mm h^{-1} for MWINX – R plot. Again, there is a wide spread in the probability distributions, particularly for the scattering signatures, *i.e.*, in PCT_{85} – R plots. For the emission signature [Figs.8(a) & 9(a)], the relatively narrower spread in the probability distribution reinforce the notion that emission signature is more directly related to surface rainfall rate than scattering signature. However, its insensitivity for higher rainfall rate makes it necessary to incorporate scattering signatures for rainfall retrievals. Because of the large scatter between PCT_{85} and rainfall rate, the rainfall rate retrieved from scattering signatures would have a larger random error. The relation and probability distribution between MWINX and rainfall rate are also included in the Figs. 8 and 9. It is seen that MWINX provides a smooth transition from emission-dominant light rain regime to scattering-dominant heavy rain regime.

5. Structures of rain clouds

5.1. *Vertical profiles of precipitation*

Given the same surface rainfall rate, how are the precipitating particles (raindrops and large ice particles) distributed vertically? With the availability of the TRMM PR data, we are able to shed some light on this question. The results of mean precipitation profiles shown in Fig. 10 were generated using TRMM PR 2A25 data for the monsoon region during the period from 1 June through 30 September 1999. Each profile in the figure is an average of those profiles whose rainfall rate at 2-km altitude is

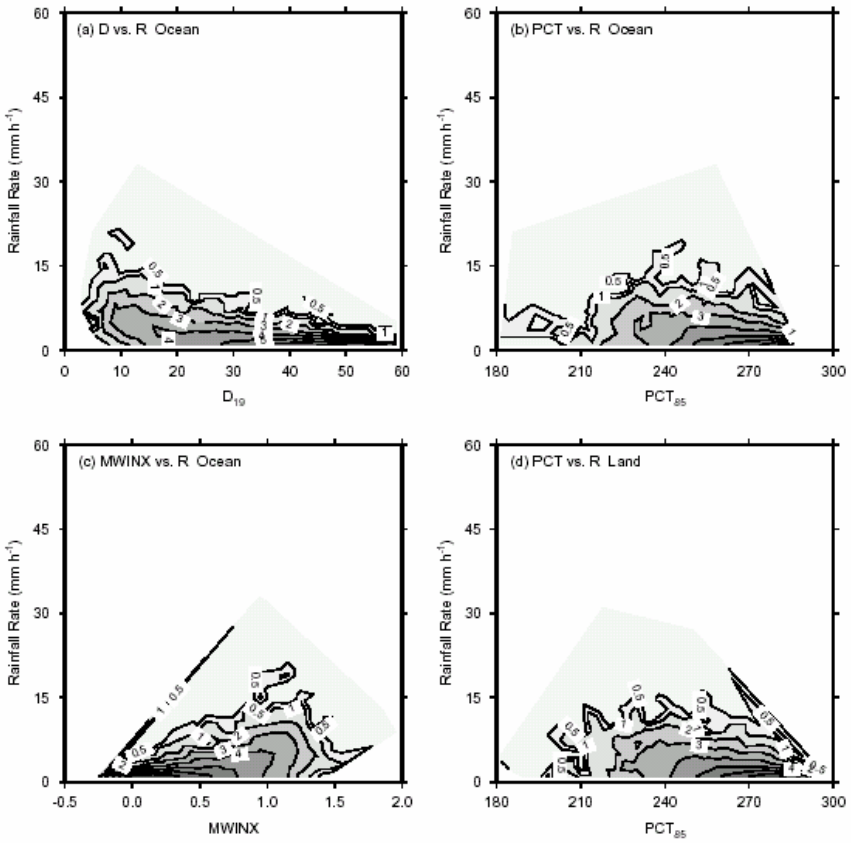

Figs. 9(a-d). Same as Fig. 8 except for stratiform rain pixels

around (within ±1 mm h^{-1}) the values shown below the curves. We divided all precipitating profiles into 4 categories by rain and surface types, *i.e.*, convective over land, stratiform over land, convective over ocean and stratiform over ocean. The number of profiles that are used for the averaging is 343120, 1103828, 332786 and 881685, respectively, for the four categories.

From Fig. 10, we may draw the following conclusions. For stratiform rains, the freezing level near 5 km separates two totally different profile patterns. Below the freezing level, rainfall rates are almost constant with height for profiles over both ocean and land, implying that raindrops experience no significant growth or evaporation. For profiles with surface rainfall rate greater than 10 mm h^{-1}, downward toward surface there is a slight decrease of rainfall rate for land profiles while there is a slight increase for oceanic profiles. But these variations are far less than those seen in the convective profiles. Above the freezing level, a sharp drop off occurs in the first 1 km layer, followed by a slower variation above. This feature has been observed and explained by previous investigators (Houze, 1993, Chapter 6). It is explained that while falling from above, ice particles grow mainly by vapor deposition at high level, which is the slowest microphysical growth mode. While they are falling near the freezing level, the ice particles may grow by deposition, riming, and more importantly, aggregation. The last process increases the particle size dramatically, which in turn sharply increases the radar reflectivity.

The convective profiles are distinctly different from the stratiform profiles, and there are significant difference between oceanic and land convective profiles. Unlike stratiform rain profiles whose rainfall rate peaks near the freezing level, the maximum rainfall rate in the convective profiles appears at a lower level. This is particularly evident for profiles over ocean, of which many profiles exhibit the highest rainfall rate at 1.5 km, the lowest level used for averaging to avoid surface contamination. If we consider that the increase of rainfall rate toward lower altitude is a result of particles' growth while they fall, the further increase below freezing level suggests a substantial growth of precipitation by warm microphysical processes (coalescence), particularly for oceanic convections. Comparing Fig.10(a) with Fig.10(c), it is seen that for the same surface rainfall rate the rain-layer is deeper for profiles over land than those over ocean. In other words,

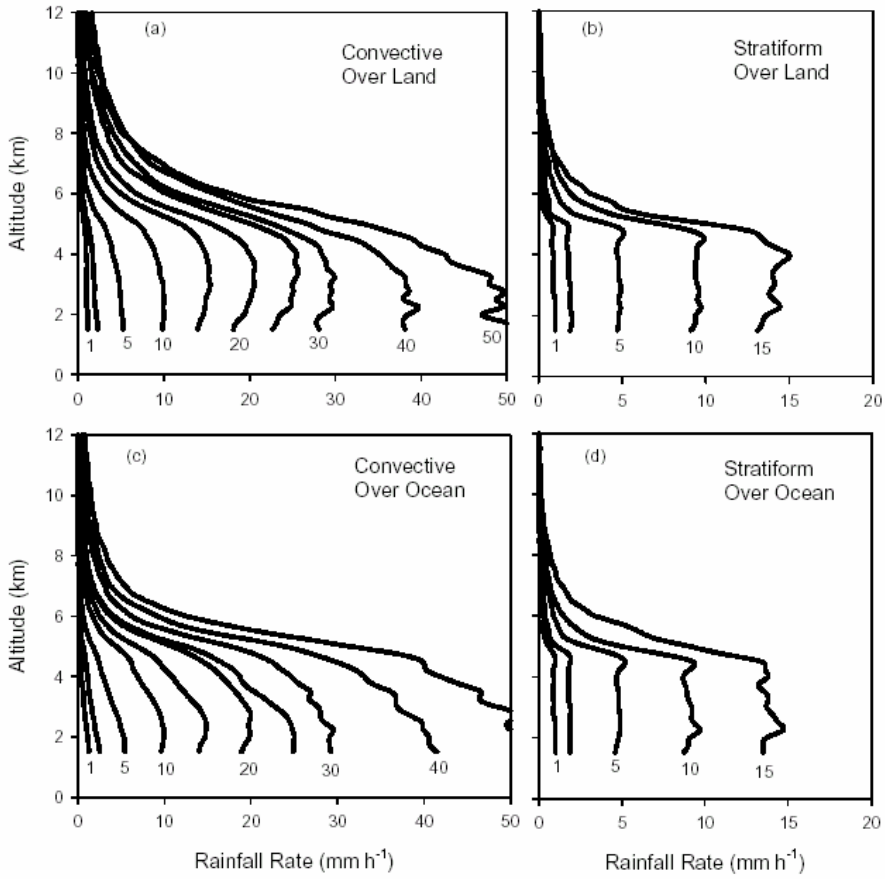

Figs. 10(a-d). Mean precipitation profiles produced using TRMM PR data. (a) convective rains over land, (b) stratiform rains over land, (c) convective rains over ocean, and (d) stratiform rains over ocean. Data are for the Indian summer monsoon region during 1 June through 30 September 1999. Note that there are significant differences between stratiform and convective rains, and between convective rains over land and over ocean

to produce the same surface rainfall rate, it requires a deeper convective cloud over land than over ocean. This is consistent with the difference in $PCT_{85} - R$ relation for convective rains between over ocean and land as shown in Fig. 7, in which we showed that given the same surface rainfall rate convective rains over land have a stronger scattering signature than rains over ocean. By examining Fig.10(a), it is found that the layer of possible coalescence growth below freezing level is very shallow, or nonexistent for land profiles, suggesting that the bulk of the growth of the rain occurs at higher altitudes. In fact, the pattern of the land profiles suggests that the major growth of precipitation occurs near and above freezing level. It is well known that lightning associated with convective clouds almost exclusively occurs over land areas (Zipser and Lutz, 1994). Because in-cloud electrification is an indication of supercooled water drops, it is plausible that a strong updraft exists above the freezing level in over-land convections, which sustains a substantial amount of cloud liquid water and a fast growth of precipitation near and above the freezing level. Another feature of the land convective rain profiles is the drop off of rainfall rate toward surface, which is an indication of evaporation of raindrops.

The departure of individual profiles from the mean may be presented by the standard deviation of those profiles used to calculate the mean profile. The profiles of the standard deviation are shown in Fig. 11 arranged in the same fashion as the mean profiles shown in Fig. 10. Because we used 2-km rainfall rate as reference to calculate mean profiles, the standard deviation at that level is the smallest. In general, heavier rains also display greater variability in terms of standard deviation. Given the same surface rainfall rate, the largest difference among profiles occurs around the freezing level at ~5 km regardless surface and rain type, reflecting that complicated microphysical processes around the melting layer. Similar to the mean values, the variability of rainfall

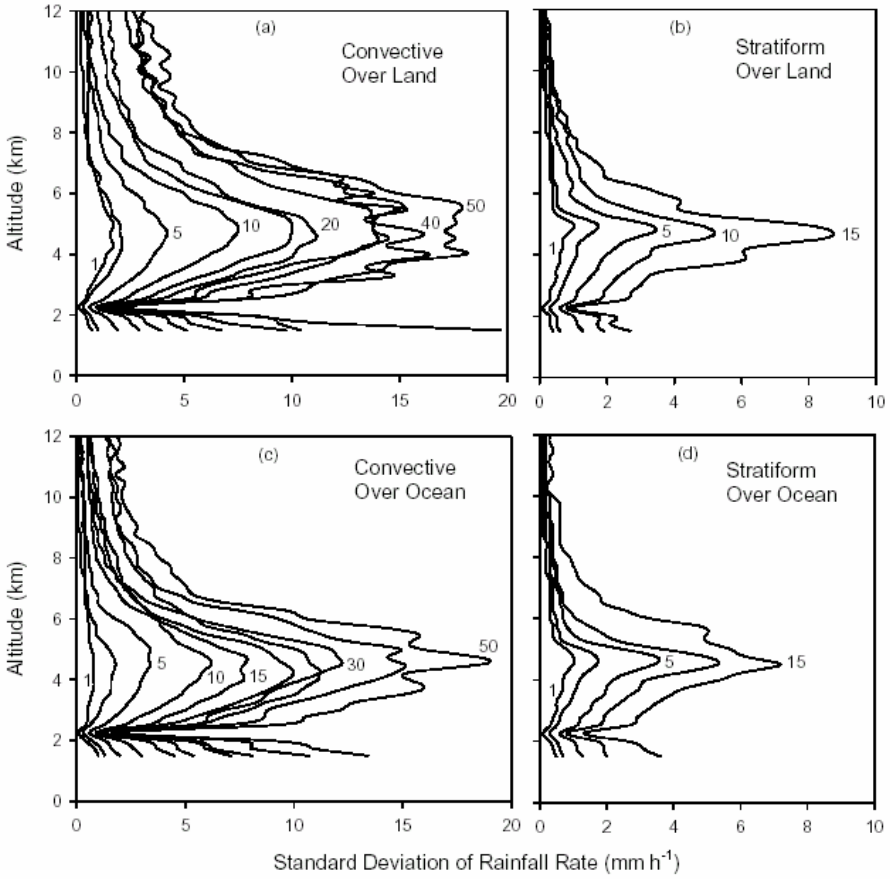

Figs. 11(a-d). The profiles of standard deviation of precipitation for (a) convective rains over land, (b) stratiform rains over land, (c) convective rains over ocean, and (d) stratiform rains over ocean

rates above the freezing level is also larger for over land rain events than for over ocean rain events.

5.2. *Horizontal inhomogeneity of rain field*

Comparing Fig. 6 with Fig. 7, it is noticed that the relationships between rainfall rate and microwave signatures calculated by the plane-parallel radiative transfer model have significant differences from those observed by satellite. To further illustrate the differences, we plotted in Fig. 12 the calculated and observed relations of D_{19} and PCT_{85} *versus* rainfall rate. The open and solid circles are observations, respectively, for stratiform and convective rains over ocean, which are the same as the circles in Figs. 7(a&b). The light lines show the results of the plane-parallel model, which is the same as the lines in Figs. 6(a&b) for deep-layer rain with ice. It is seen that while they follow the observations reasonably for stratiform rains (open circles), the plane-parallel model results have noticeable departures from the observed relations from convective rains (solid circles). The departures may be explained by the sub-pixel scale variability of rain field as follows.

Assume that the brightness temperature T_B can be expressed by rainfall rate R as $T_B = f(R)$ for a horizontally uniform rain field (plane-parallel). Due to the strong nonlinearity of this relation (for example, Wilheit *et al.*, 1977), generally, $\overline{T}_b \neq f(\overline{R})$ where the over-bar denotes averaging over the field-of-view, if rainfall rates are not uniformly distributed within the satellite pixel. The footprint size for 19.4 GHz TMI channel is about 25 km, much greater than the scale of individual convective cells, which is on the order of a few kilometers. Therefore, the sub-pixel inhomogeneity effect will drive the actually observed T_B – R relation away from the one modeled under the plane-parallel assumption. The greater the sub-pixel inhomogeneity is, the further the departure will be. Because stratiform rains are generally more uniform than convective ones, the microwave signature *versus* rainfall rate relations observed for stratiform rains are much closer to the modeled results than those for convective rains (Fig. 12).

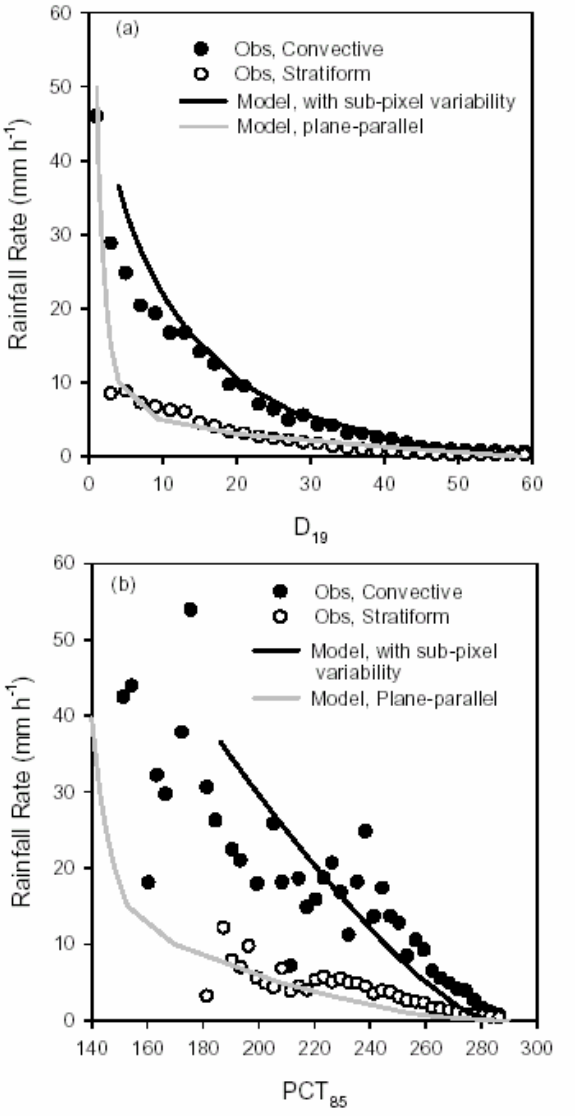

Figs. 12(a&b). Comparison between model simulation and satellite observation for (a) D_{19} *versus* rainfall rate over ocean and (b) PCT_{85} *versus* rainfall rate over ocean. Solid and open circles are observations. Light lines are plane-parallel model results and dark lines are model results with inclusion of sub-pixel inhomogeneity of rain field

Given a sufficiently large number of samples, rainfall rates can often be represented by a lognormal distribution (Wilheit *et al*., 1991):

$$p(R)\mathrm{d}R = \frac{1}{\sigma_R\sqrt{2\pi}} \exp\left\{\frac{-[\ln(R/R_0)]^2}{2\sigma_R^2}\right\}\frac{\mathrm{d}R}{R}, \qquad (3)$$

where $p(R)$ is the probability distribution function, R_0 is the mode rainfall rate and the σ_R is the variance of the rainfall rates. Dividing the area covered by a satellite pixel into many smaller sub-areas and assuming that rainfall rates from these sub-areas follow the lognormal distribution, we may calculate T_Bs for the each sub-area using the plane-parallel model and then average T_Bs of all sub-areas to find $\overline{T}_B$. Also, the averaged rainfall rate of the pixel may be calculated by $\overline{R} = R_0 \exp(\sigma_R^2/2)$. Using the field-of-view averaged brightness temperature and rainfall rate, we may generate the relations of $\overline{D}_{19}$ *versus* $\overline{R}$ and $\overline{PCT_{85}}$ *versus* $\overline{R}$ to compare them with observations. The relations so produced were also shown in Fig. 12 by dark curves. It is seen that with the inclusion of the sub-pixel variability of the rain field, the results generated by the radiative transfer model are much closer to observations for convective rains. Therefore, we may conclude that, for convective rains, the horizontal inhomogeneity of the rainfall field has played the vital role in determining the relations between microwave signatures and rainfall rate.

In deriving the field-of-view averaged relations shown in Fig. 12, we needed to specify the variance σ_R in Eqn.(3). Unfortunately, there is no observational data to derive it for the monsoon region focused in this study. Instead, we used a parameterization based on 4-month surface radar data from the Tropical Ocean Global Atmosphere Coupled Ocean Atmosphere Response Experiment (TOGA COARE). This dataset contains hourly rain maps with a 2 km by 2 km resolution (Short *et al*., 1997). The variance so derived for a 24 km spatial scale (similar to TMI 19.4 GHz pixel size) can be written as

$$\sigma_R = 1.1 + 8.9\times10^{-2}r + 1.6\times10^{-2}r^2 + 5.7\times10^{-3}r^3 - 3.1\times10^{-3}r^4, \qquad (4)$$

where $r = \ln(R_0)$. Although the variance used here is derived from another region, Fig. 12 shows that the difference between plane-parallel model results and actual observations can be reasonably explained by the sub-pixel variability of rain field.

6. Conclusions

The purpose of this study has been to identify the cloud and precipitation features in the Indian summer monsoon region based on satellite microwave and infrared observations. The methodology consists of a mixture of observational data analyses and radiative transfer model

simulation, whereas it is attempted to understand the observed signatures by comparing them with model results. Emphases are particularly put on the differences between stratiform and convective rains and between rains over land and over ocean.

On average, rains cover 6 to 9% percent of the analyzed Indian summer monsoon area with a slight higher rain area fraction over land than over ocean, although the mean rainfall rate over the two surface types are essentially the same. Mean convective rainfall rate is about 6 times higher than mean stratiform rainfall rate while the latter covers 4 to 5 times more area than the former. As a results, convective rains produce high rain total than stratiform rains with a ratio of about 3:2. Over oceanic areas, we were able to examine the relations between microwave emission and scattering signatures. The former reflects the amount of liquid and the latter reflects the amount of ice water in an atmospheric column. It is found that there is a significant correlation between the two signatures, implying that liquid water (mostly below freezing level) and ice water amounts generally increase or decrease in a coherent fashion over a scale of the satellite footprint. This finding, on one hand, underscores the importance of cloud ice in producing surface rainfall, on the other hand, lays the physical ground for determining surface rainfall using microwave scattering signatures, which is the only measurable signature over land areas from microwave measurements.

The relations between rainfall rate and satellite observed radiative signatures have been examined using data measured by TRMM satellite. The difference between convective and stratiform rains in these relations is evident virtually by any measures – cloud top temperature, microwave emission, scattering and combined signatures. Stratiform rains are generally weaker than convective ones although their cloud tops may reach a comparable height. Cloud top temperature (or height) appears no skill to reflect surface rainfall rates for stratiform rains while colder cloud top temperatures tend to correspond to higher rainfall rates for convective clouds. As rainfall rate increases, microwave emission signature reaches saturation (*i.e.*, D_{19}~0) much quicker for stratiform rains than for convective rains. Again, similar to cloud top temperature, the skill for relating scattering signature to surface rainfall rate is minimal for stratiform rains while stronger scattering signatures (smaller PCT_{85}) clearly tend to correspond to higher rainfall rates for convective rains. Additionally, the rainfall rate – scattering signature relation shows a distinct difference between convective rains over land and over ocean. Corresponding the same rainfall rate, the scattering signature over land is about twice as high as that over ocean.

The aforementioned differences arise because of the different vertical and horizontal structures among rains of different types. The mean vertical precipitation profiles generated from TRMM radar showed that stratiform rains have a relatively simpler pattern with a constant rainfall rate below freezing level and a sharp drop-off above, regardless over land or ocean. Convective rain profiles, on the other hand, often have the maximum rainfall rate below the freezing level, implying a significant growth of raindrops by warm microphysical processes, such as coalescence. Because of the difference in precipitation profiles, given the same surface rainfall rate there is usually less integrated liquid water in the atmospheric column for convective than for stratiform rains, resulting in a weaker emission signature [bigger D_{19}, [Fig. 7(a)] for convective rains. It is also found that given the same surface rainfall rate, the amount of ice particles above freezing level is substantially greater for convective rains over land than over ocean, which explains the difference of scattering signatures between rains over the two different surface types. Horizontal inhomogeneity of rain field also plays an important role in determining the relations between surface rainfall rate and satellite received microwave signatures. Due to the sub-pixel variability of rains, the results of plane-parallel models differ from actual observations. Using a variance model derived from surface radar observations during TOGA COARE, we demonstrated that the model results were able to match the observations qualitatively by including the sub-pixel variability.

Important lessons may be learned from the examination of the satellite signatures, particularly the microwave signatures. The characteristics of rain clouds revealed from this study are not only useful to understand the nature of precipitation process, but also helpful in future development of satellite cloud and precipitation retrieval algorithms. Both are important for documenting and forecasting monsoon weather and monsoon events.

Acknowledgements

TRMM satellite data were provided by NASA Goddard Distributed Active Archive Center. This research has been supported by NASA TRMM grant NAG5-8647 and NSF grant ATM-0002860.

References

Adler, R. F., Kidd, C., Petty, G., Morrissey, M., Goodman, M. H., 2001, "Intercomparison of Global Precipitation Products: The Third Precipitation Intercomparison Project (PIP-3)", *Bull. Am. Meteorol. Soc*., **82,** 1377-1396.

Adler, R. F., and Negri, A. J., 1988, "A satellite infrared technique to estimate tropical convective and stratiform rainfall", *J. Appl. Meteorol*., **27**, 30-51.

Arkin, P. A. and Meisner, B. N., 1987, "The relationship between large-scale convective rainfall and cold cloud over the Western Hemisphere during 1982-84", *Mon. Wea. Rev.*, **115**, 51-74.

Arkin, P. A. and Xie, P., 1994, "The Global Precipitation Climatology Project: First Algorithm Intercomparison Project", *Bull. Am. Meteorol. Soc*., **75,** 401-419.

Awaka, J., Iguchi, T. and Okamoto, K., 1998, "Early results on rain type classification by the Tropical Rainfall Measuring Mission (TRMM) precipitation radar", *Proc. 8th URSI Commission F Open Symp*., Averior, Portugal, Union Radio-Scientifigue Internationale, 134-146.

Houze, R. A., 1993, "*Cloud Dynamics*", Academic Press, New York, p573.

Huffman, G. J., Adler, R. F., Rudolf, B., Schneider, U. and Keehn, P. R., 1995, "Global precipitation estimates based on a technique for combining satellite-based estimates, rain gauge analysis, and NWP model precipitation information", *J. Clim.*, **8**, 1284-1295.

Iguchi, T. and Meneghini, R., 1994, "Intercomparison of single-frequency methods for retrieving a vertical rain profile from airborne or spaceborne radar data", *J. Atmos. Oceanic Technol.*, **11**, 1507-1516.

Krishnamurti, T. N., Surendran, S., Shin, D. W., Correa-Torres, R. J., Kumar, T. S. V. V. and Williford, E., Kummerow, C., Adler, R. F., Simpson, J., Kakar, R., Olson, W. S. and Turk, F. J., 2001, "Real-time multianalysis–multimodel superensemble forecasts of precipitation using TRMM and SSM/I products", *Mon. Wea. Rev*., **129**, 2861-2883.

Kummerow, C., Simpson, J., Thiele, O., Barnes, W., Chang, A. T. C., Stocker, E., Adler, R. F. and Hou, A., Kakar, R., Wentz, F. and Ashcroft, P., Kozu, T., Hong, Y., Okamoto, K., Iguchi, T. and Kuroiwa, H., Im, E. and Haddad, Z., Huffman, G., Ferrier, B. and Olson, W. S., Zipser, E., Smith, E. A., Wilheit, T. T. and North, G., Krishnamurti, T. and Nakamura, K., 2000, "The Status of the Tropical Rainfall Measuring Mission (TRMM) after Two Years in Orbit", *J. Appl. Meteorol*., **39**, 1965-1982.

Liu, G.,1998, "A fast and accurate model for microwave radiance calculations", *J. Meteor. Soc. Japan,* **76**, 335-343

Liu, G., 2002, "Satellite remote sensing: Precipitation", In *Encyclopedia of Atmospheric Sciences*, J. Holton, J. Pyle, and J. Curry, ed., Academic Press, New York. (*in press*).

Liu, G. and Curry, J. A., 1993, "Determination of characteristic features of cloud liquid water from satellite microwave measurements", *J. Geophys. Res*., **98**, 5069-5092.

Liu, G., and Curry, J. A., 1998, "An investigation of the relationship between emission and scattering signals in the SSM/I data", *J. Atmos. Sci*., **55**, 1628-1643.

Liu, G., and Fu, Y., 2001, "The characteristics of tropical precipitation profiles as inferred from satellite radar measurements", *J. Meteor. Soc.* Japan, **79**, 131-143.

Liu, G., Curry, J. A. and Sheu, R. S., 1995, "Classification of clouds over the Western Equatorial Pacific Ocean using combined infrared and microwave satellite data", *J. Geophys. Res*., **100**, 13811-13826.

Petty, G. W., 1994, "Physical retrievals of over-ocean rain rate from multichannel microwave imaging. Part I: Theoretical characteristics of normalized polarization and scattering indices", *Meteor. Atmos. Phys*., **54**, 79-100.

Ramanathan, V. and Collins, W., 1991, "Thermodynamic regulation of ocean warming by cirrus clouds deduced from observations of the 1987 El Niño", *Nature*, **351**, 27-32.

Rossow, W. B. and Schiffer, R. A., 1991, "ISCCP cloud data products", *Bull. Am. Meteorol. Soc.*, **72**, 2-20.

Short, D. A., Kucera, P. A., Ferrier, B. S., Gerlach, J. C., Rutledge, S. A. and Thiele, O. W., 1997, "Shipborne radar rainfall patterns within the TOGA/COARE IF", *Bull. Am. Meteorol. Soc.*, **78**, 2817-2836.

Simpson, J., Adler, R. F. and North, G. R., 1988, "A proposed Tropical Rainfall Measuring Mission (TRMM) satellite", *Bull. Am.. Meteorol. Soc*., **69**, 278-295.

Smith, E. A., Lamm, J. E., Adler, R., Alishouse, J., Aonashi, K., Barrett, E., Bauer, P., Berg, W., Chang, A., Ferraro, R., Ferriday, J., Goodman, S., Grody, N., Kidd, C., Kniveton, D., Kummerow, C., Liu, G., Marzano, F., Mugnai, A., Olson, W., Petty, G., Shibata, A., Spencer, R., Wentz, F., Wilheit, T. and Zipser, E., 1998, "Results of WetNet PIP-2 Project", *J. Atmos. Sci*., **55**, 1483-1536.

Spencer, R. W, Goodman, H. M. and Hood, R. E., 1989, "Precipitation retrieval over land and ocean with the SSM/I: Identification and characteristics of the scattering signal", *J. Atmos. Oceanic Technol*., **6**, 254-273.

Wilheit, T. T., Chang, A. T. C., Rao, M. S. V., Rodgers, E. B. and Theon, J. S., 1977, "A satellite technique for quantitatively mapping rainfall rates over the oceans", *J. Appl. Meteorol.*, **16**, 551-560.

Wilheit, T. T., Chang, A. T. C. and Chiu, L. S., 1991, "Retrieval of monthly rainfall indices from microwave radiometric measurements using probability distribution functions", *J. Atmos. Oceanic Technol*., **8**, 118-136.

Wilheit, T., Adler, R., Avery, S., Barrett, E., Bauer, P., Berg, W., Chang, A., Ferriday, J., Grody, N., Goodman, S., Kidd, C., Kniveton, D., Kummerow, C., Mugnai, A., Olson, W., Petty, G., Shibata, A. and Smith, E., 1994, "Algorithms for the retrieval of rainfall from passive microwave measurements", Remote Sensing Rev., **11**, 163-194.

Zipser, E. J. and Lutz, K. R., 1994, "The vertical profile of radar reflectivity of convective cells: A strong indicator of storm intensity and lightning probability?", Mon. Wea. Rev., **122**, 1751-1759.